High-throughput morphological chirality quantification of twisted and wrinkled gold nanorods

High-Throughput Morphological Chirality Quantification of Twisted and Wrinkled Gold Nanorods

Evgenii Vlasov[1‡], Wouter Heyvaert[1‡], Bing Ni[2], Kyle Van Gordon[3], Robin Girod[1], Johan Verbeeck[1], Luis M. Liz-Marzán[3,4,5,6], Sara Bals[1]*

[1]EMAT and NANOlab Center of Excellence, University of Antwerp, 2020 Antwerp, Belgium

[2]Physical Chemistry, University of Konstanz, Universitätsstrasse 10, 78457 Konstanz, Germany

[3]CIC biomaGUNE, Basque Research and Technology Alliance (BRTA), 20014 Donostia-San Sebastián, Spain

[4]Centro de Investigación Biomédica en Red, Bioingeniería, Biomateriales y Nanomedicina (CIBER-BBN), 20014 Donostia-San Sebastián, Spain

[5]Ikerbasque, Basque Foundation for Science, 48009 Bilbao, Spain

[6]CINBIO, University of Vigo, 36310 Vigo, Spain

*E-mail: Sara.Bals@uantwerpen.be

KEYWORDS Chirality, Nanoparticles, Morphology, Scanning transmission electron microscopy, Secondary electron imaging, Electron beam induced current

ABSTRACT

Chirality in gold nanostructures offers an exciting opportunity to tune their differential optical response to left- and right-handed circularly polarized light, as well as their interactions with biomolecules and living matter. However, tuning and understanding such interactions demands quantification of the structural features that are responsible for the chiral behavior. Electron tomography (ET) enables structural characterization at the single particle level and has been used to quantify the helicity of complex chiral nanorods. On the other hand, the technique is time-consuming and consequently lacks statistical value. To address this issue, we introduce herein a high-throughput methodology that combines images acquired by secondary electron electron beam-induced current (SEEBIC) with quantitative image analysis. As a result, the geometric chirality of hundreds of nanoparticles can be quantified in less than one hour. When combining the drastic gain in data collection efficiency of SEEBIC with a limited number of ET data sets, a better understanding on how the chiral structure of individual chiral nanoparticles translates into the ensemble chiroptical response can be reached.

Nanostructures can present chiral features at multiple scales, from atomic up to submicron scale. The identification and implementation of chirality in inorganic nanoparticles (NPs) has given rise to a new class of materials having the intriguing property of not being superimposable to their mirror images, with promising applications.[1–4] Metallic chiral NPs in particular have received growing interest because of their unique chiroptical properties. Structural features resulting from different synthetic approaches have been found to show a significant variation, but in general the scales of the chiral features are in the nanometer range.[5–8] The surface plasmon resonance of metal chiral NPs, which corresponds to the collective oscillations of electrons driven by light, results in

strong near-field enhancement, optical absorption maxima at the resonance wavelength and, in turn, unusually high optical activity.[9] Dissymmetry factors quantified by the differential extinction (absorption plus scattering) of left- and right-handed circularly polarized light now reach up to 40% for Au NPs,[8] orders of magnitude higher than chiral molecules. Recent reports have demonstrated that chiral metal NPs are excellent candidates for biosensing,[10–12] separation,[13–15] catalysis,[16–18] treatment of diseases,[19–21] and photonics.[22–24] However, reliable implementation of these and other applications requires a much deeper understanding of the connection between NP morphology and optical activity.

A broad range of synthesis procedures have been proposed to transfer chirality to inorganic NPs.[3–5,7,25,26,6,27,28] Among these, colloidal synthesis is arguably the most promising route because of its scalability and low cost. However, the unavoidable polydispersity in colloidal systems also increases the variability of the often complex morphology of chiral NPs. To comprehend structure-property relations for these systems that exhibit geometrical chirality at nanoscale, high-resolution characterization of the nanoscale features at the single particle level is required. Additionally, extrapolation of single-particle properties to the ensemble level, while considering polydispersity, demands high-throughput analysis of the chiral NP morphology, so that average structural descriptors can be extracted with adequate statistical rigor. Tomography in transmission electron microscopy (TEM), or electron tomography (ET), is an excellent tool to study three-dimensional (3D) structure of NPs,[29] and therefore to analyze the chiral features at the nanoscale. In a typical ET measurement, a series of 50-100 high-angle annular dark-field scanning transmission electron microscopy (HAADF-STEM) images are acquired while tilting the sample over an as-large-as-possible tilt range (approximately ±75°). Mathematical algorithms, such as the simultaneous iterative reconstruction technique (SIRT), can then be used to retrieve the 3D morphology of the

NP. Based on the obtained 3D reconstructed data sets, further quantification is possible, *e.g.* through our recently reported quantitative methodology to objectively characterize the helical morphology of Au nanorods (NR).[30,31] In short, this method is based on analyzing a 3D reconstruction volume of a chiral Au NR and its corresponding surface mesh. For each surface element, the orientation of the normal vector is computed with respect to the helical axis, and measurements at a given radius and orientation are integrated over the surface of the NR. In this manner, a "helicity function" is defined, which can be interpreted as a measure for the distribution of helical inclination angles of the surface features of a given NR.

A drawback of this methodology originates from the extremely time-consuming nature of ET, which limits the number of NRs that can be investigated in practice. Acquisition times of 1 hour per particle are not uncommon, even though recent developments have enabled reducing acquisition time down to a few minutes, using more advanced tomography approaches.[32,33] Nonetheless, also the data processing and reconstruction steps that follow after the tilt series acquisition are time-consuming. Consequently, one can typically analyze approximately 10 NPs in a timeframe of one day. We thus aimed to increase significantly the throughput of structural quantification for the difficult case of quantifying nanoscale chiral morphology in Au NRs, for which we decided to exploit imaging by secondary electron electron beam induced current (SEEBIC) in STEM.[34,35] This technique uses the generation of secondary electrons (SEs) in a TEM and can be considered as an unusual modification of the electron beam-induced current (EBIC) setup,[36] which is typically used for the study of the buried junctions or defects in semiconductors, or for the examination of charge carrier properties, both in SEM[37] and STEM.[38] The measured current in SE-based EBIC (SEEBIC current) arises from holes generated by the emission of SEs from the sample, upon interaction with the primary beam. This measured current is equal and

opposite to the generated SE signal and can be mapped pixel-by-pixel to produce an image. Since SEs originate from near-surface regions of the samples, the SEEBIC image intensity is sensitive to variations in surface topography, as recently demonstrated for achiral NPs.[35] SEEBIC images therefore strongly resemble SEM images, often used to investigate chiral NPs, but with the advantage of improved spatial resolution (**Figure S1**). Although SE based images can even be acquired with atomic resolution, we demonstrate herein the use of SEEBIC images for high-throughput quantification of helical features with sizes in the nanometer range within the morphology of chiral Au nanorods.

RESULTS AND DISCUSSION

Three different types of Au NRs were analyzed, each yielding a twisted or "wrinkled" morphology. Sample 1 is a left-handed sample of twisted Au NRs, which have large diagonal edges with 4-fold symmetry and were synthesized using *D*-cysteine as a chiral inducer, as described by Ni *et al.* (**Figure 1a, d, g** and **Figure S1a, d**).[6] Samples 2 and 3 are wrinkled Au NRs synthesized as described by González-Rubio *et al.* (**Figure 1 (d-i)** and **Figure S1b, c, e, f**).[7] These two samples were synthesized with different *(S)*- and *(R)*- enantiomers of 1,1′-binaphthyl-2,2′-diamine (BINAMINE), using single crystalline Au NR seeds. We refer the reader to references [6] and [7], respectively, for detailed information on the synthesis procedures. The left column in **Figure 1** shows 2D projections of representative NRs, acquired using HAADF-STEM, a standard technique to investigate nanoparticles.

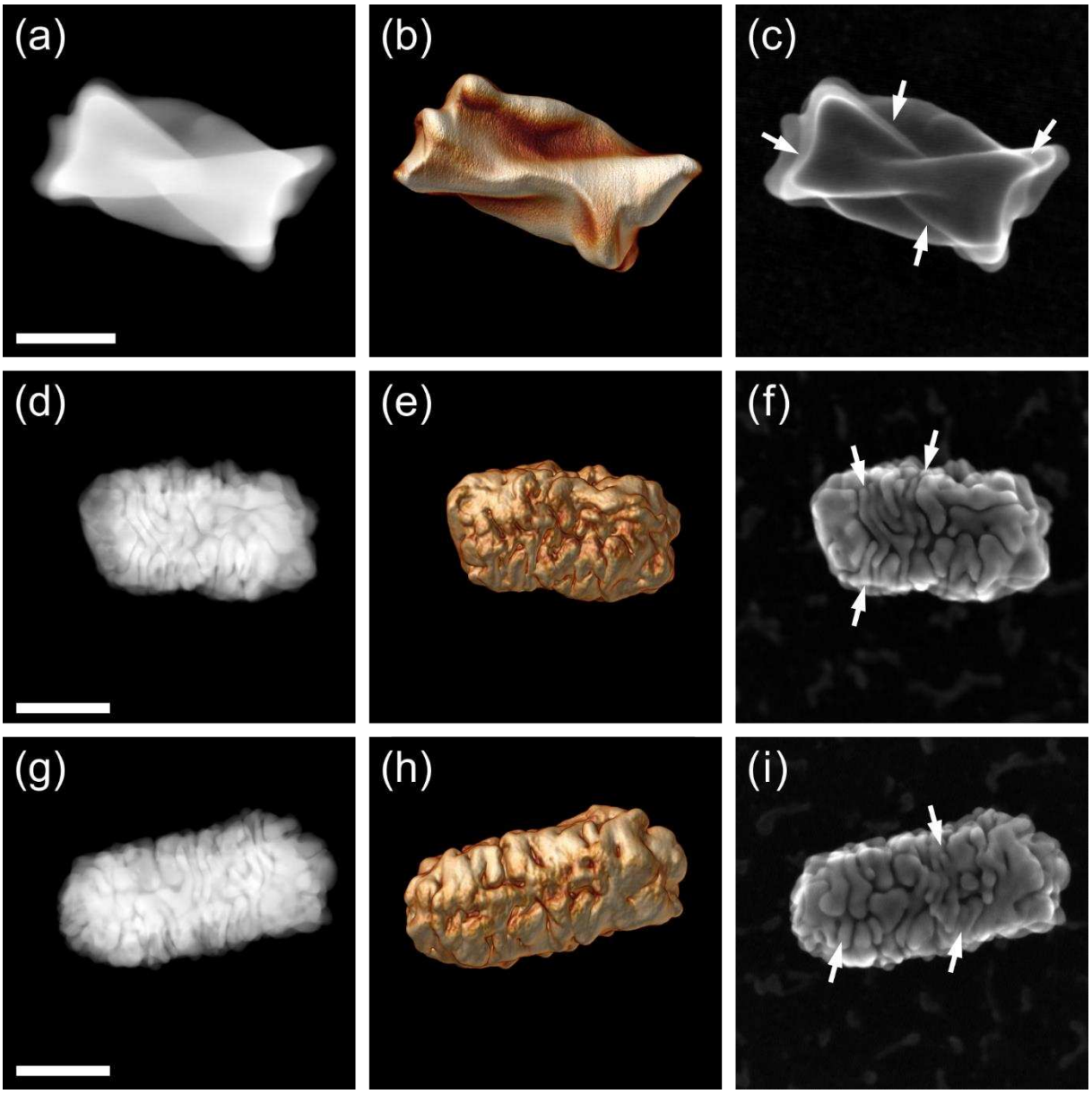

Figure 1. High-magnification (a, d, g) HAADF-STEM, (b, e, h) ET visualizations, and (c, f, i) SEEBIC images of a representative particle for (a-c) sample 1, (d-f) sample 2, and (g-i) sample 3. White arrows indicate discrepancies between SEEBIC and ET data. Scale bars are 50 nm.

Next, we compared the 3D characterization of selected NPs by ET (**Figure 1**, middle column) with those using the SEEBIC method (right column). The main concept of SEEBIC in comparison to conventional ET is schematically described in **Figure 2**. As explained above, SEEBIC relies on

the detection of current arising from holes generated by the emission of SEs from the sample (**Figure 2b**). SEs are electrons with typical energies below 50 eV, ejected from the sample during inelastic interactions with the primary electron beam. Due to their extremely low mean free path (0.5 nm for Au[39]), the SE signal originates from the near-surface region of the sample. The SE signal is sensitive to the topography of nanostructures because its contrast mainly originates from a dependence of the SE yield on the surface inclination angle and the so-called "edge effect". The former indicates that the SE yield is high when the surface is steeply inclined with respect to the electron beam, whereas the "edge effect" introduces high SE intensities when SEs are emitted from a tip or an edge of the specimen. The SEEBIC signal can be mapped as a function of the probe position, to produce an image that directly depends on the SE yield for each scan position.

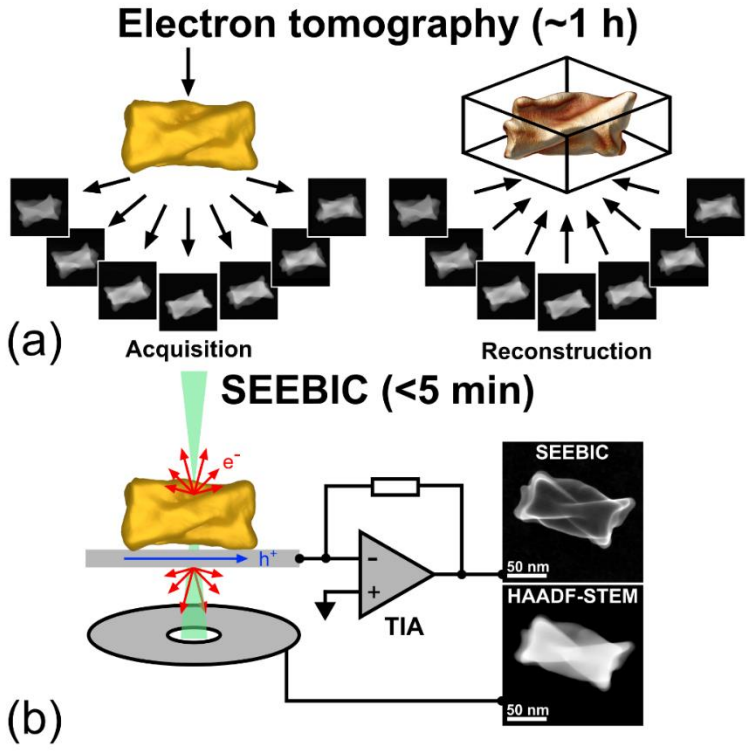

Figure 2. Schematic description of the working principles of (a) ET, (b) SEEBIC. Red arrows in panel b indicate directions of SE emission from the NP surface; the blue arrow indicates the net hole current flowing into the TIA input.

The obtained SEEBIC images of chiral NRs in **Figure 1** are in close agreement with the results of ET experiments. For the latter, a tilt series of 51 HAADF-STEM images (with an approximate total acquisition time of about 1 hour) was used as input for 3D reconstruction, whereas the SEEBIC image was acquired in less than 5 minutes. Minor discrepancies between HAADF, SEEBIC and ET are also noticeable, which we attribute to three main effects: backside contribution, imperfect ET reconstructions and projection overlap. First, a typical assumption is that SEEBIC contrast predominantly originates from the NP surface and more specifically the top one, as most SEs generated at the bottom of the NP are reabsorbed by the support film. However, as seen in **Figure 1c** (white arrows), a contribution from the bottom surface cannot be fully prevented because of gaps created by the helical ridges that provide an escape way for SEs (**Figure S2**).[35] As further explained in the discussion on quantification of helicity, this effect has little impact on the overall statistics. The second type of discrepancies is seen in samples 2 and 3, where white arrows (**Figure 1f, i**) indicate minor discrepancies between SEEBIC and ET, corresponding to a lack of wrinkled features in the ET reconstruction. This is likely related to imperfections during the ET process, *e.g.*, resulting from missing wedge artifacts, which are known to result in a reduction of the reconstruction resolution and leading to blurring of the reconstructed volume (see **Figure S3**).[40] Finally, we also observed that the wrinkled features of samples 2 and 3 appear sharper in the HAADF-STEM images, in comparison to the ET reconstructions and SEEBIC images. As illustrated in **Figure S4** this is likely the result of overlapping of the features in projection images and not due to electron beam damage (**Figure S5**).

Figure 1 illustrates that SEEBIC images provide a visualization of the surface morphology of twisted NPs with at least similar quality as that obtained by ET, but with a drastic gain in data collection efficiency. This gain can be further improved by selecting a relatively low magnification

(see below), taking into account the overall size of the NPs, as well as the characteristic size of the structural features at their surface. In this manner, every SEEBIC image may display multiple particles dispersed on a TEM support, so that SEEBIC imaging of hundreds of NRs per hour becomes possible. The imaging magnification needs to be optimized so that all the relevant structural features can be distinguished from the image, while keeping a sufficient number of NPs located within the field of view. For example, the samples studied in the current work have comparable particle sizes, but samples 2 and 3 have smaller surface features than those in sample 1 and therefore a higher magnification is required to resolve them (**Figures S6-S8**).

Once SEEBIC images of hundreds of NRs have been acquired, their helicity can be readily analyzed. To this aim, we modified a methodology that was previously reported by our group to quantify the morphology of chiral NRs, based on ET experiments.[30] Our current workflow is visualized in **Figure 3**. The particles are first localized in HAADF-STEM images and SEEBIC images are simultaneously acquired (**Figure 2b**). In HAADF-STEM images, the NPs appear bright against a dark background. Using Otsu thresholding,[41] followed by a connected-components analysis,[42] the particle shapes are then segmented, and their outlines transferred to the corresponding SEEBIC images (**Figure 3**). Next, the long axis of the NRs is defined by fitting an ellipse to the segmentation results. This axis is assumed to correspond to the helical axis of the NR during further quantification. Then, the gradient of the intensity of the SEEBIC image is calculated to obtain, for each pixel, the gradient magnitude and its orientation with respect to the direction of the helical axis. The gradient orientation is defined in the image plane as a polar angle so that 0° and 180° degrees are perpendicular to the helical axis. We remap the orientation in the range [-90°, +90°], ultimately yielding the helical inclination angle α of the surface features for a given NR (**Figure 3**). Due to the "edge effect" of the SE signal and the dependence of the SE yield on

the surface inclination angle, the magnitude of the gradient in SEEBIC images can be considered as a measure for the "steepness" of the surface.[35] Therefore, to give more importance to well-defined topological features, which are encoded in the intensity changes of the SEEBIC image, we further attribute a weight to each pixel, corresponding to its gradient magnitude. For quantification (**Figure 3**), the NR helical structure can then be presented as a weighted histogram of the obtained inclination angles. To accurately describe the handedness of a structure, we define the helicity function $H(\alpha)$ as the sum between the histogram bins with right-handed (positive) inclination angles and those with left-handed (negative) inclination angles. As such, the helicity function will be positive for a given value of α if the structure is dominantly right-handed at this inclination angle and *vice versa*. Importantly, these helicity histograms can be readily aggregated over many particles to yield the average plot of helicity and orientation in a polydisperse sample. In addition, and as we previously reported for ET, each histogram of a particle or of an ensemble can be integrated over the orientation range. This yields a single, easily interpretable value representing the total helicity of a particle H_{seebic} or of a sample H_{avg}.[30] This value will be -1 for ideally left-handed structures, 0 for non-helical structures, and +1 for perfect right-handed structures.

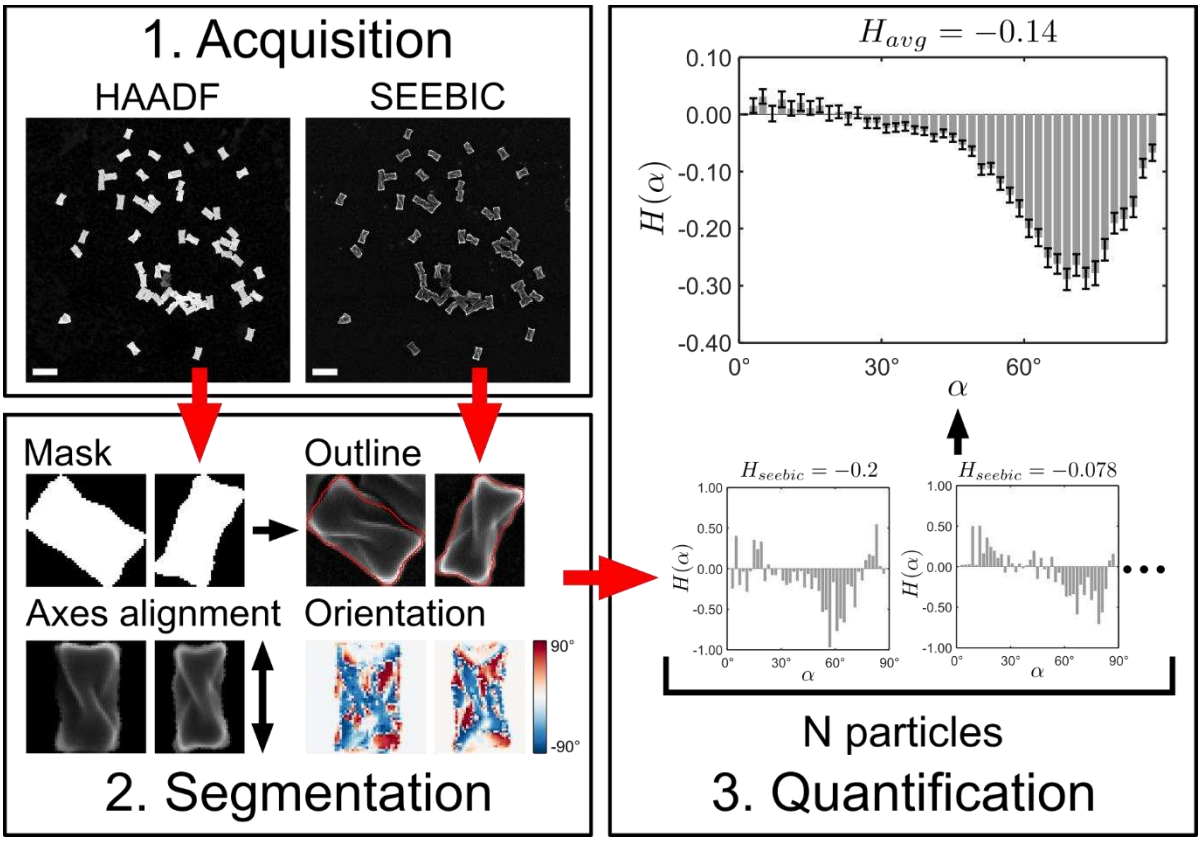

Figure 3. Proposed workflow to quantify the helical morphology of NRs imaged by simultaneous HAADF-STEM and SEEBIC acquisitions. First, a SEEBIC image and a HAADF-STEM image are acquired simultaneously at low magnification. Next, the NRs in the HAADF-STEM image are segmented to separate their projected shapes from the background and a connected-components analysis is used to identify individual NRs (red boundaries). The helical inclination angle α is calculated from the gradient of the SEEBIC image. Finally, the helicity function is calculated separately for each NR, and all results are averaged to retrieve the helicity function of the ensemble. The total helicity H_{avg} can be calculated by integrating the helicity function for all NRs. Average helicity plot shows the data obtained from N particles, error bars represent standard error for each data bin. Scale bars are 500 nm.

We first evaluated our method for helicity quantification by comparing optical characterization at the ensemble level (**Figure 4 and S9**) with SEEBIC average helicity (**Figure 5-7**). Optical activity plots (**Figure 4**) show the differential absorption of right- and left-handed polarized light as a function of wavelength, normalized by the total absorption. The positive peak *g*-factors for samples 1 and 3 indicate they are optically left-handed in the spectral range of the peak (preferential absorption of left-handed polarized light) and a negative *g*-factor for sample 2 shows that it is optically right-handed in the spectral range of the peak. For SEEBIC characterization, seven images of sample 1 were acquired at a magnification of 28.5 k× (corresponding to a total field of view of approximately 2700 × 2700 nm^2), to analyze 327 NRs. For samples 2 and 3, fourteen and twelve SEEBIC images were acquired at a magnification of 57 k× (field of view of approximately 1300 × 1300 nm^2), to analyze 174 and 348 NRs, respectively. A complete overview of all SEEBIC images can be found in **Figures S6-S8**. From this analysis, the total average helicity was calculated to be -0.14 for sample 1 **(Figure 5a**), +0.033 for sample 2 (**Figure 6a**), and -0.039 for sample 3 (**Figure 7a**), indicating an average left-handed geometry for samples 1 and 3 and a right-handed one for sample 2. These results are in excellent agreement with the optical characterization and demonstrate that SEEBIC-based average helicity calculations are adequately describing the optical handedness of the ensemble.

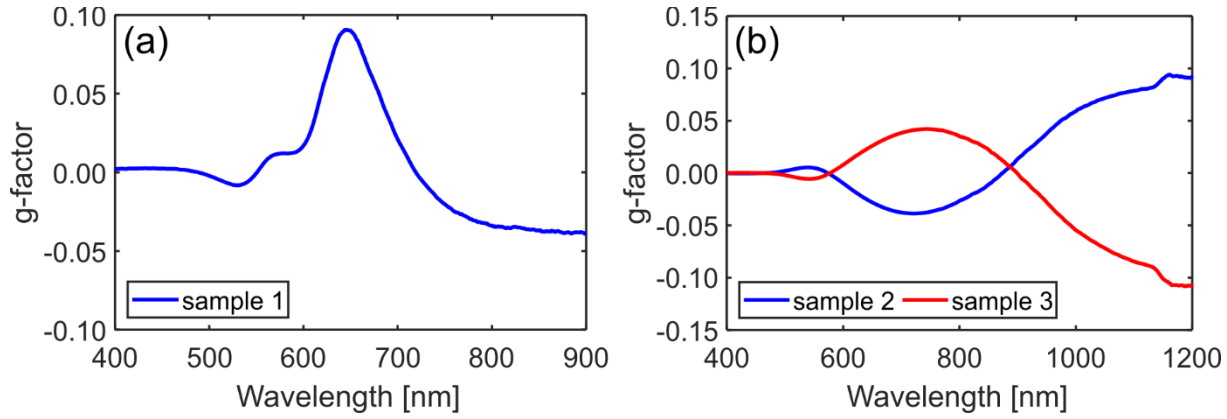

Figure 4. Optical activity (*g*-factor) plots for the studied samples: (a) sample 1, (b) samples 2 and 3.

Next, we compared the results of SEEBIC ensemble (**Figures 5a, 6a, 7a**) and single-particle (**Figures 5c, 6c, 7c**) helicity quantification with our previous approach based on the ET reconstruction for a single NR (**Figures 5b, 6b, 7b**).[30] A detailed description of the latter approach is provided in the **Supporting information, section 5**. The ET helicity plots show a distribution of chiral features, indicating the prevailing handedness at various distances from the helical axis and inclination angles. In other words, the approach "unwraps" a chiral NR layer-by-layer, such that the higher the radius (ρ), the closer the feature is located to the NR surface. The helicity function here is encoded in colors: red for right-handed (positive helicity function), blue for left-handed (negative helicity function) morphological features. As with SEEBIC, the plots can be integrated over the radius and orientation ranges to yield a pseudoscalar descriptor of the total helicity, H_{tomo}. While not strictly equal due to the differences in their calculation, the SEEBIC values (H_{seebic} or H_{avg}) and the total helicity from ET data H_{tomo} both integrate the orientation of surface features of chiral NPs and should therefore be correlated. To simplify the interpretation of ET-based quantification results and their comparison with results based on SEEBIC imaging, the dimensionality of the data can be reduced by integrating the helicity function $H(\alpha, \rho)$ over the

radius of the NP (**Figure S10**). This will enable a direct comparison with SEEBIC helicity quantification results.

For sample 1, the angular distribution of helical features in **Figure 5a** shows that the predominant left-handed helical features in these particles are oriented with rather steep inclination angles, around 70°, whereas right-handed features with low inclination angles are also present. The analysis based on the ET reconstruction of a representative NR, shown in **Figure 5b and Figure S10a**, also shows predominant left-handed features with angles around 60° (cloud of blue data points indicated with a blue arrow in the histogram) and a mixture of right- and left-handed features with small inclination angles (indicated with a red arrow in the histogram). This comparison demonstrates that quantification of the average structure using the SEEBIC approach for sample 1 is in good agreement with ET data. The main left-handed peak of the angular distributions in **Figure 5a, b** corresponds to the diagonal edges of the NRs, whereas right-handed low-angle peaks can be attributed to the contribution of the edges on the NR tips (see **Supporting information, Figures S11-S13**). At the single particle level, tip edges do not appear to have a preferred orientation (see **Figure 5b, c** and **Figure S11**), however, averaging over a large ensemble (327 particles) shows that they are predominantly right-handed. Quantitative data obtained from a SEEBIC image of the same NR used for ET are shown in **Figure 5c.** Good agreement was found with both ensemble averaged data obtained through SEEBIC and the results obtained by ET as negative helicity values were obtained.

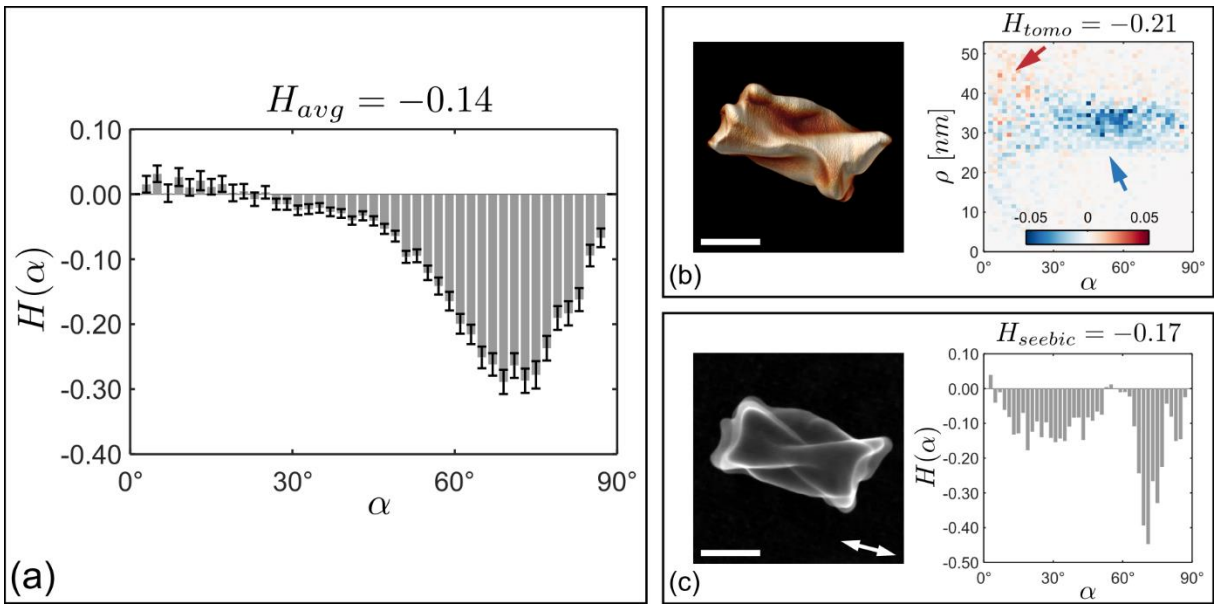

Figure 5. Results of chirality quantification for sample 1. (a) Helicity quantification of a NR ensemble, based on seven overview SEEBIC images; (b) Helicity analysis from an ET reconstruction of a single particle; (c) Helicity analysis based on the SEEBIC image of the same particle. Plots in panels (a) and (c) show the angular distributions of morphological chiral features for the NRs present in the SEEBIC images. The average helicity plot shows the data obtained from 327 particles, error bars represent the standard error for each data bin. The helicity function plotted in (b) shows the distribution of morphological chiral features, with various inclination angles and distances from the helical axis of the NR in the ET reconstruction. The plot in panel (b) is color-coded: red for right-handed, blue for left-handed morphological features. Helicity quantification from ET data was achieved using the approach introduced in ref. [30]. The orientation of the helical axis in panel (c) is indicated by a double-headed arrow. Scale bars are 50 nm.

Sample 2 yields an average right-handed morphology, with a maximum of angular distribution around 50−60° (**Figure 6a**). This correlates well with ET-based quantification results, thereby demonstrating the diffuse distribution of mainly right-handed features in the histogram, as shown by the red arrow in **Figure 6b**. Both SEEBIC ensemble-averaged and ET-based results also show

a presence of features with mixed handedness, oriented with low inclination angles (<30°) (blue arrow in **Figure 6b**). Thorough analysis of the experimental data (**Figures S14, S15**) did not reveal a strong influence of edges, tips or SEEBIC artefacts on the orientation maps and on the helicity plots at the level of a single particle. From the standard error in **Figure 6a**, it can be seen that these specific features are randomly distributed and cancel out each other's contribution when averaged over a large ensemble. In terms of absolute helicity, both SEEBIC and ET methods at the single particle level as well as the ensemble SEEBIC measurement reveal a less helical character than sample 1 with a 5-10 fold decrease in value. This again demonstrates the good correlation between the SEEBIC and ET approaches. Interestingly, the decrease in helicity also correlates with a lower peak *g*-factor (**Figure 4b**), again showing the value of helicity measurements to link morphological chirality with optical properties.

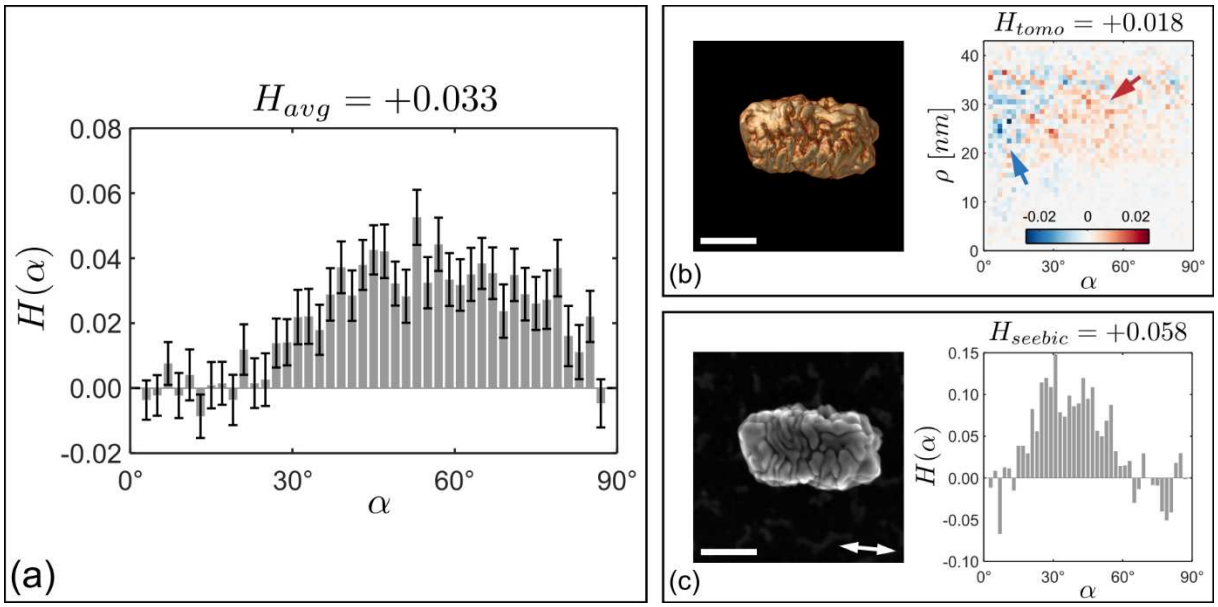

Figure 6. Results of chirality quantification for sample 2. (a) Helicity quantification of a NR ensemble, based on fourteen overview SEEBIC images; (b) Helicity analysis from an ET reconstruction of a single particle; (c) Helicity analysis based on the SEEBIC image of the same particle. Plots in panels (a) and (c) show the angular distributions of morphological chiral features

for the NRs present in SEEBIC images. The average helicity plot shows the data obtained from 174 particles, error bars represent the standard error for each data bin. The helicity function plotted in (b) shows the distribution of morphological chiral features with various inclination angles and distances from the helical axis of the NR in the ET reconstruction. The plot in panel (b) is color-coded: red for right-handed, blue for left-handed morphological features. Helicity quantification from ET data was achieved using the approach introduced in ref. [30]. The orientation of the helical axis in panel (c) is indicated by a double-headed arrow. Scale bars are 50 nm.

Sample 3, on the other hand, shows an average left-handed structure (**Figure 7a**), in agreement with the analysis based on ET (**Figure 7b and Figure S10c**). However, the latter additionally shows the presence of both left- and right-handed features with small inclination angles (shown with a red arrow), which are located close to the NR surface (note high values of ρ for these features).

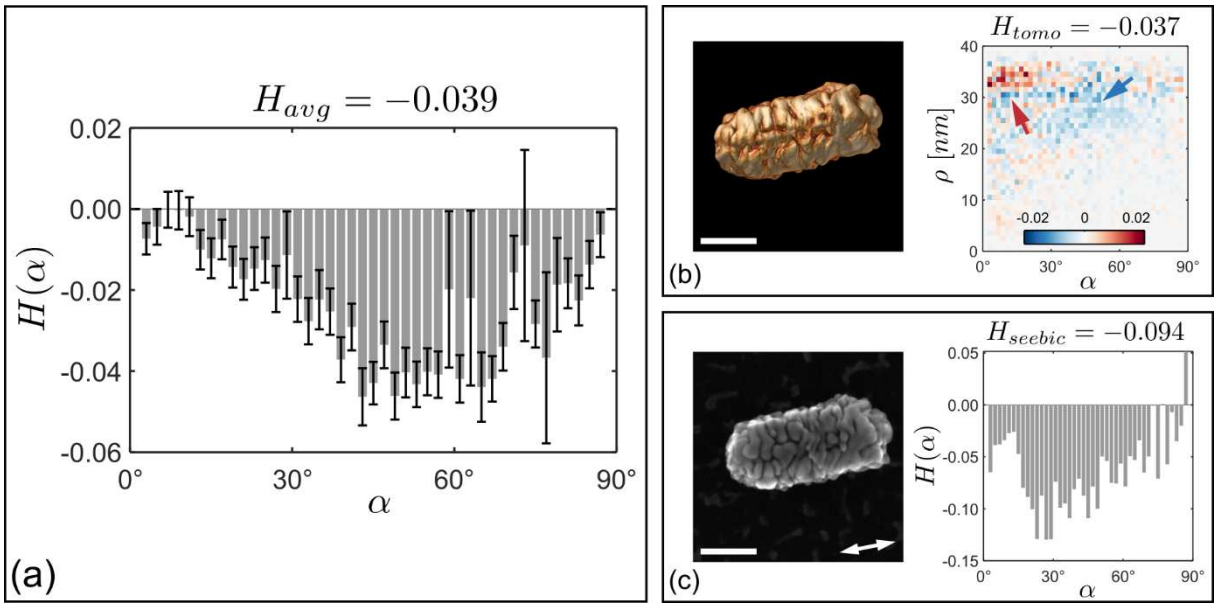

Figure 7. Results of chirality quantification for sample 3. (a) Helicity quantification of a NR ensemble based on twelve overview SEEBIC images; (b) Helicity analysis from an ET reconstruction of a single particle; (c) Helicity analysis based on the SEEBIC image of the same

particle. Plots in panels (a) and (c) show the angular distributions of morphological chiral features for the NRs present in SEEBIC images. The average helicity plot shows the data obtained from 348 particles, error bars represent the standard error for each data bin. The helicity function plotted in (b) shows the distribution of morphological chiral features with various inclination angles and distances from the helical axis of the NR in the ET reconstruction. The plot in panel (b) is color-coded: red for right-handed, blue for left-handed morphological features. Helicity quantification from ET data was achieved using the approach introduced in ref. [30]. The orientation of the helical axis in panel (c) is indicated by a double-headed arrow. Scale bars are 50 nm.

Despite the fact that quantification results for the average SEEBIC data and single-particle ET are globally matching, we find minor discrepancies in positions and intensities of the peaks in the distributions. The observed difference can be understood in terms of morphological variations among individual particles. We thus conclude that individual ET reconstructions of single NRs are not always representative of the sample batch. This is not surprising because ET is indeed a very local technique, and this consideration is crucially important for a general understanding of the connection between structure and chiroptical properties. SEEBIC imaging is proposed as a route to overcome this limitation because the technique also enables local characterization, but at a higher throughput.

Although SEEBIC images are generally in good agreement with ET reconstructions, it is important to point out that inconsistencies may occur. For example, **Figure 8a** shows mixed handedness compared to both ensemble-averaged SEEBIC (**Figure 5a**) and ET data (**Figure 8b**). Quantification results obtained from the SEEBIC image of a single NR in this case, show the presence of right-handed features with low inclination angles (<30°) and very high inclination angles (>80°), which are less obvious or even absent in quantification results based on ET. The

right-handed morphological features in **Figure 8a** have a contribution that is higher than the contribution of the left-handed features turning a positive total helicity value (H_{seebic}) that contradicts ensemble-averaged results (H_{avg}). In this case, the signature of the right-handed features is attributed to the contribution of the edges on NR tips (see **Supporting Information - Section 6** and **Figures S11-S13** for details) and artifactual contrast due to the contribution of the backside of the NPs to the overall SEEBIC signal. It should be noted that the right-handed features appearing in SEEBIC images due to the contrast from the backside have little influence on average structure quantification because they are suppressed by a significantly higher contribution of the left-handed features, as shown by the high absolute value and low standard error at ~70° in the ensemble plots (**Figure 5a)**.

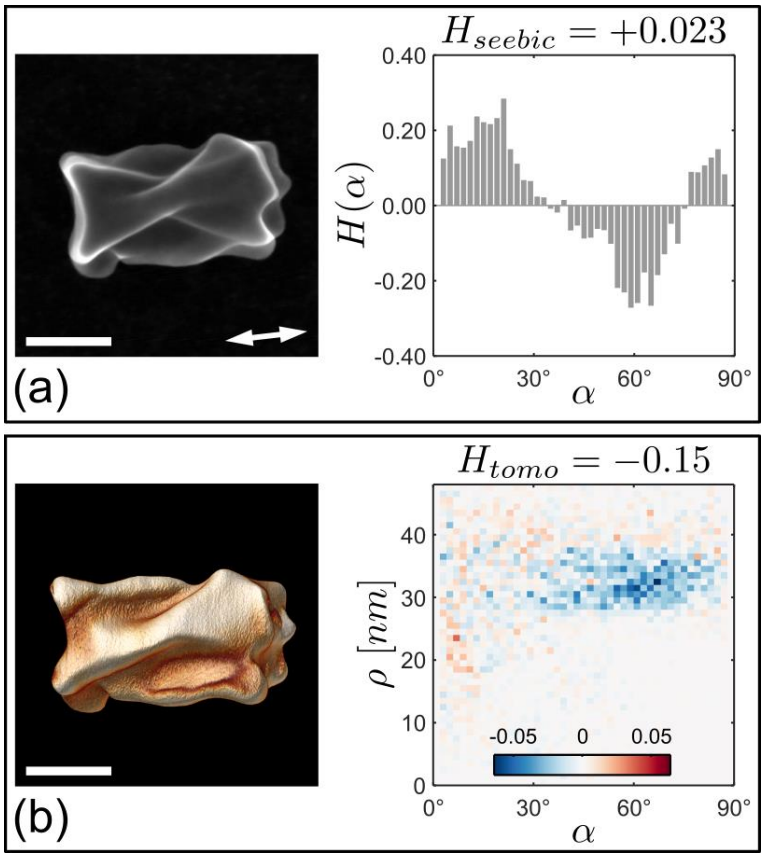

Figure 8. Results of helicity quantification for sample 1 showing the discrepancy between quantitative data obtained from (a) a single SEEBIC image and (b) an ET reconstruction. The plot in panel (a) shows the angular distributions of morphological chiral features present in the obtained SEEBIC image. The orientation of the helical axis in panel (a) is indicated by a double-headed arrow. The helicity function plotted in (b) shows the distribution of morphological chiral features with various inclination angles and distances from the helical axis of the NR in ET reconstructions. The plot in panel (b) is color-coded: red for right-handed, blue for left-handed morphological features. Helicity quantification from ET data was achieved using the approach introduced in ref. [30]. Scale bars are 50 nm.

For sample 2, inconsistencies can also exceptionally be noted, *e.g.*, when comparing **Figure 9a** to **Figure 6a** and **Figure 9b**. In this case, the difference can be explained by a random distribution of nanoparticles on the support film, so that the top side of a specific NR has a predominant left-handed orientation, whereas the average NR morphology is right-handed. A volume render obtained from the ET reconstruction along the same viewing direction as the one for which the SEEBIC image was acquired, results in this NP visually appearing as a left-handed morphology (**Figure S16**). However, 3D renders from different orientations reveal predominantly right-handed morphologies (see **Figure S16**). The presence of features with different handedness corresponds to the idea that inorganic chiral NPs can yield a continuum of chiral features, which is in stark contrast to *e.g.*, amino acids presenting binary chirality. It is thus important to acquire SEEBIC images or ET data sets from multiple NRs, to investigate the overall chirality coming from the ensemble of individual NRs in a given sample. The advantage of SEEBIC over ET is the possibility of acquiring the data with higher throughput. On the other hand, ET enables the investigation of the distribution of chiral features for entire NRs, whereas SEEBIC is currently only able to show

the chiral morphology at the top surface. By combining HAADF-STEM and SEEBIC images of a given NR, it might be possible to extract a 3D mesh of the entire surface, but further work is required to reach this goal.

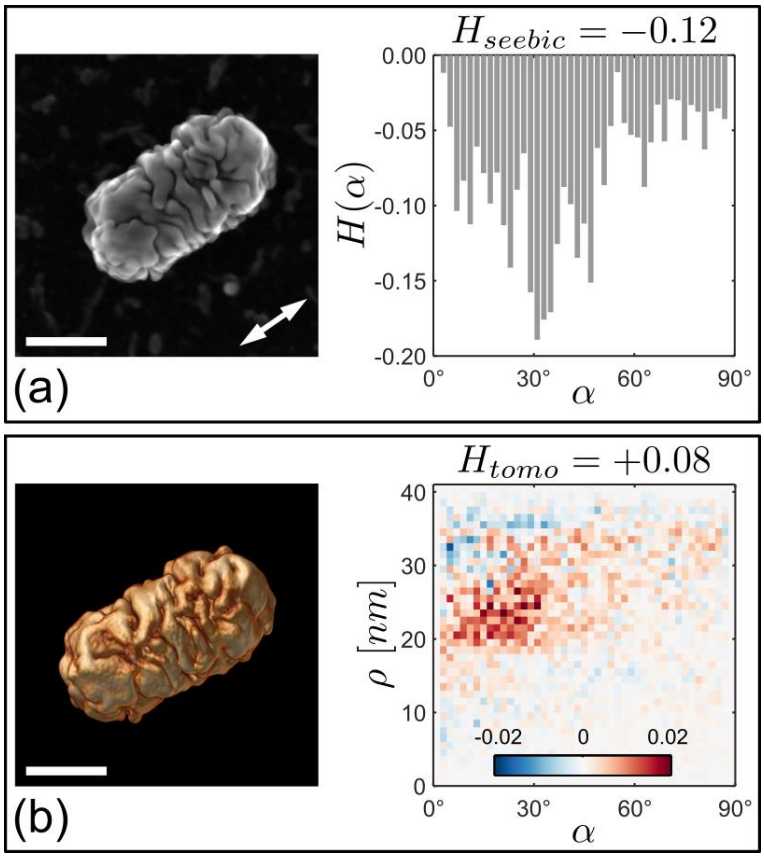

Figure 9. Results of helicity quantification for sample 2, showing the discrepancy between quantitative data obtained from (a) single SEEBIC image and (b) ET reconstruction. The plot in panel (a) shows the angular distributions of morphological chiral features present in the obtained SEEBIC image. The orientation of the helical axis in panel (a) is indicated by a double-headed arrow. The helicity function plotted in (b) shows the distribution of morphological chiral features with various inclination angles and distances from the helical axis of the NR in the ET reconstruction. The plot in panel (b) is color-coded: red for right-handed, blue for left-handed

morphological features. Helicity quantification from ET data was achieved using the approach introduced in ref. [30]. Scale bars are 50 nm.

We finally investigated how the variability in SEEBIC measurements at the single particle level affected the ensemble measurements. **Figure 10a** (see **Figure S14** for the complete overview) shows arbitrarily oriented NRs with a variety of morphologies, which are representative of sample 2. The results of helicity quantification, based on these images, demonstrate that some NRs show chiral features that are characterized by low angles (~30°), whereas others demonstrate opposite or even mixed handedness (**Figure 10a**). However, averaging arbitrarily oriented NRs over an ensemble (in this case comprising 174 NPs), results in cancelling low-angle features with opposite handedness (see **Figure 10b**) leading to the distribution shown in **Figure 10c**, where a high-angle (~40-70°), right-handed morphology is predominant. It is likely that these high-angle features determine the optical properties measured by ensemble techniques (**Figure 4**). Plots showing a transition from the morphologies of single NRs to an average ensemble structure for samples 1 and 3 are provided as **Supporting information** (**Figures S11, S17 and S18a, c**). Our results show that, to fully retrieve information about both the average structure of a sample and the local NP morphology, and how these aspects are connected, a combination of multiple overview SEEBIC images and a few ET data sets will be required.

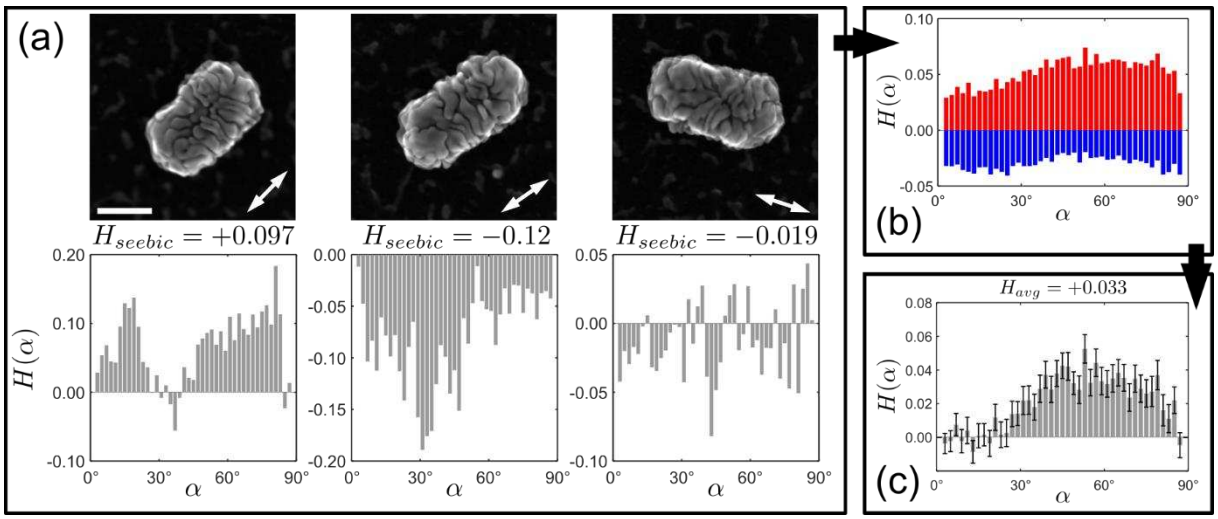

Figure 10. Illustration of how morphologies of single NRs translate to an average morphology of the ensemble for sample 2. (a) SEEBIC images of single NRs with the results of their quantification. (b) Results of helicity quantification of a NR ensemble, based on overview SEEBIC images for left-handed and right-handed features. Plots are encoded in colors: red for right-handed and blue for left-handed morphological features. (c) Helicity quantification of a NR ensemble, based on overview SEEBIC images with indicated standard error. The orientation of the helical axis in panel (a) is indicated by a double-headed arrow. Scale bar is 50 nm.

CONCLUSIONS

We have shown that the helical morphology of chiral Au NRs, with significant polydispersity at the level of surface features (twists and wrinkles) can be efficiently quantified using high-throughput SEEBIC measurements. This approach overcomes the limitation of poor statistics obtained by ET, which is limited to analyzing only a few particles per sample batch because of long acquisition and processing times. By exploiting SEEBIC in combination with a dedicated quantification procedure to measure helicity, we were able to gain insights into the ensemble-level

(chiral) characteristics of twisted and wrinkled nanoparticles within a timeframe of one experimental day. We found that the average helicity values, calculated for hundreds of NRs per sample batch were in good agreement with the optical properties of the sample, confirming that helicity measurements enable linking the nanoscale morphology with the chiroptical handedness. Further, we confirmed the robustness of the SEEBIC helicity quantification, showing that edge and backside effects are averaged out at the ensemble level. This accurate and statistically relevant morphological information combined with local characterization provides a route to connect ensemble properties to the morphologies of single NPs.

EXPERIMENAL METHODS

ET data were acquired over a tilt range of ±72°, with tilt increments of 3°, using an aberration-corrected "cubed" Thermo Fisher Themis Z TEM, operated at an acceleration voltage of 200 kV and a beam current of 50 pA. Reconstructions of the tilt series were performed using the SIRT algorithm implemented in ASTRA Toolbox 1.90[43] for MATLAB 2022b. Visualization of 3D reconstructions was carried out using the Amira 5.4.0 software.

SEEBIC imaging at the single-particle level was performed at an acceleration voltage of 200 kV and a beam current of 500 pA. A custom-made transimpedance amplifier (TIA) with a total gain of 2×10^9 V/A and a bandwidth of 8 kHz, electrically connected to the sample via a DENS Solutions Wildfire holder, was used to convert the SEEBIC signal into a voltage signal digitized by the Attolight OUDS II scan engine, along with the amplified HAADF-STEM detector signal. No image filtering was applied during post-processing. High-throughput SEEBIC data were acquired at an acceleration voltage of 60 kV and a beam current of 500 pA. SEEBIC images of 1024×1024 pixels were acquired with a dwell time of 200 µs, leading to a total acquisition time of

approximately 3.5 minutes per image. HAADF-STEM images were acquired simultaneously with SEEBIC and used for automatic segmentation during the data processing step.

Previous studies have demonstrated the use of MEMS devices with electron-transparent Si_3N_4 windows and lithographically patterned electrodes to perform SEEBIC experiments.[34,44,45] It was demonstrated that the Si_3N_4 membrane yields sufficient conductivity for the required charge transport.[34] Alternatively, conventional TEM grids can also be used for SEEBIC experiments.[35,44] We used herein a sample carrier based on a 0.6 mm thick FR4 printed circuit board, designed to fit in a DENS Solutions Wildfire heating holder, which allows the use of a conventional copper TEM grid as a sample support.[35]

It is well-known that low-energy SEs can be absorbed by carbon layers of just a few nm in thickness. Therefore, after drop-casting onto a copper TEM grid, the samples were cleaned with Ar/O_2 plasma (3:1) to avoid the build-up of a carbon contamination layer during the acquisition of SEEBIC data, as well as to remove surface ligands potentially hindering topography imaging.

It should be noted that the acquisition of SEEBIC single-particle images requires an electron dose comparable with that accumulated during a conventional ET experiment.[35] Such a high electron dose may lead to beam damage or material re-shaping. To rule out the effect of electron beam damage on the NP shape during SEEBIC imaging, HAADF-STEM images were acquired both before and after SEEBIC experiments (**Figure S5**).

ASSOCIATED CONTENT

Supporting Information

Supporting information includes additional experimental data, supplementary figures and their discussion (PDF). Supporting movies used for inspection of particle morphology (MP4). This material is available free of charge via the Internet at http://pubs.acs.org.

AUTHOR INFORMATION

Corresponding Author

*E-mail: Sara.Bals@uantwerpen.be

Author Contributions

‡E.V. and W.H. contributed equally. The manuscript was written through contributions of all authors. All authors have given approval to the final version of the manuscript.

ACKNOWLEDGMENT

The authors acknowledge financial support by the European Research Council (ERC CoG No. 815128 REALNANO to S.B.) and from MCIN/AEI/10.13039/501100011033 (Grant PID2020-117779RB-I00 to L.M.L.-M and FPI Fellowship PRE2021-097588 to K.V.G.). Funded by the European Union under Project 101131111 – DELIGHT. JV acknowledges the eBEAM project supported by the European Union's Horizon 2020 research and innovation program FETPROACT-EIC-07-2020: emerging paradigms and communities.

ABBREVIATIONS

ET, electron tomography; SEEBIC, secondary electron electron beam induced current; NP, nanoparticle; CD, circular dichroism; TEM, transmission electron microscopy; 3D, three-dimensional; HAADF-STEM, high-angle annular dark-field scanning transmission electron microscopy; SIRT, simultaneous iterative reconstruction technique; NR, nanorod; SE, secondary electron; EBIC, electron beam-induced current; BINAMINE, 1,1′-binaphthyl-2,2′-diamine; TIA, transimpedance amplifier.

REFERENCES

(1) Kotov, N. A.; Liz-Marzán, L. M.; Weiss, P. S. Chiral Nanostructures: New Twists. *ACS Nano* **2021**, *15*, 12457–12460.

(2) Wang, F.; Yue, X.; Ding, Q.; Lin, H.; Xu, C.; Li, S. Chiral Inorganic Nanomaterials for Biological Applications. *Nanoscale* **2023**, *15*, 2541–2552.

(3) Cho, N. H.; Guerrero-Martínez, A.; Ma, J.; Bals, S.; Kotov, N. A.; Liz-Marzán, L. M.; Nam, K. T. Bioinspired Chiral Inorganic Nanomaterials. *Nat. Rev. Bioeng.* **2023**, *1*, 88–106.

(4) Liu, X.; Du, Y.; Mourdikoudis, S.; Zheng, G.; Wong, K.-Y. Chiral Magnetic Oxide Nanomaterials: Magnetism Meets Chirality. *Adv. Opt. Mater.* **2023**, *11*, 2202859.

(5) Lee, H.-E.; Ahn, H.-Y.; Mun, J.; Lee, Y. Y.; Kim, M.; Cho, N. H.; Chang, K.; Kim, W. S.; Rho, J.; Nam, K. T. Amino-Acid- and Peptide-Directed Synthesis of Chiral Plasmonic Gold Nanoparticles. *Nature* **2018**, *556*, 360–365.

(6) Ni, B.; Mychinko, M.; Gómez-Graña, S.; Morales-Vidal, J.; Obelleiro-Liz, M.; Heyvaert, W.; Vila-Liarte, D.; Zhuo, X.; Albrecht, W.; Zheng, G.; González-Rubio, G.; Taboada, J. M.; Obelleiro, F.; López, N.; Pérez-Juste, J.; Pastoriza-Santos, I.; Cölfen, H.; Bals, S.; Liz-Marzán, L. M. Chiral Seeded Growth of Gold Nanorods Into Fourfold Twisted Nanoparticles with Plasmonic Optical Activity. *Adv. Mater.* **2023**, *35*, 2208299.

(7) González-Rubio, G.; Mosquera, J.; Kumar, V.; Pedrazo-Tardajos, A.; Llombart, P.; Solís, D. M.; Lobato, I.; Noya, E. G.; Guerrero-Martínez, A.; Taboada, J. M.; Obelleiro, F.; MacDowell, L. G.; Bals, S.; Liz-Marzán, L. M. Micelle-Directed Chiral Seeded Growth on Anisotropic Gold Nanocrystals. *Science* **2020**, *368*, 1472–1477.

(8) Xu, L.; Wang, X.; Wang, W.; Sun, M.; Choi, W. J.; Kim, J.-Y.; Hao, C.; Li, S.; Qu, A.; Lu, M.; Wu, X.; Colombari, F. M.; Gomes, W. R.; Blanco, A. L.; de Moura, A. F.; Guo, X.; Kuang,

H.; Kotov, N. A.; Xu, C. Enantiomer-Dependent Immunological Response to Chiral Nanoparticles. *Nature* **2022**, *601*, 366–373.

(9) Nesterov, M. L.; Yin, X.; Schäferling, M.; Giessen, H.; Weiss, T. The Role of Plasmon-Generated Near Fields for Enhanced Circular Dichroism Spectroscopy. *ACS Photonics* **2016**, *3*, 578–583.

(10) Li, S.; Xu, L.; Ma, W.; Wu, X.; Sun, M.; Kuang, H.; Wang, L.; Kotov, N. A.; Xu, C. Dual-Mode Ultrasensitive Quantification of MicroRNA in Living Cells by Chiroplasmonic Nanopyramids Self-Assembled from Gold and Upconversion Nanoparticles. *J. Am. Chem. Soc.* **2016**, *138*, 306–312.

(11) Kumar, J.; Eraña, H.; López-Martínez, E.; Claes, N.; Martín, V. F.; Solís, D. M.; Bals, S.; Cortajarena, A. L.; Castilla, J.; Liz-Marzán, L. M. Detection of Amyloid Fibrils in Parkinson's Disease Using Plasmonic Chirality. *Proc. Natl. Acad. Sci. U.S.A.* **2018**, *115*, 3225–3230.

(12) Wang, X.; Hao, J.; Cheng, J.; Li, J.; Miao, J.; Li, R.; Li, Y.; Li, J.; Liu, Y.; Zhu, X.; Liu, Y.; Sun, X. W.; Tang, Z.; Delville, M.-H.; He, T.; Chen, R. Chiral CdSe Nanoplatelets as an Ultrasensitive Probe for Lead Ion Sensing. *Nanoscale* **2019**, *11*, 9327–9334.

(13) Shukla, N.; Bartel, M. A.; Gellman, A. J. Enantioselective Separation on Chiral Au Nanoparticles. *J. Am. Chem. Soc.* **2010**, *132*, 8575–8580.

(14) Gogoi, A.; Mazumder, N.; Konwer, S.; Ranawat, H.; Chen, N.-T.; Zhuo, G.-Y. Enantiomeric Recognition and Separation by Chiral Nanoparticles. *Molecules* **2019**, *24*, 1007.

(15) Sun, X.; Wang, N.; He, Y.; Kong, H.; Yang, H.; Liu, X. Molecule-Specific Vibration-Based Chiral Differentiation of Raman Spectra Using Cysteine Modified Gold Nanoparticles: The Cases of Tyrosine and Phenylalanine. *J. Mater. Chem. B* **2021**, *9*, 7167–7171.

(16) Li, S.; Liu, J.; Ramesar, N. S.; Heinz, H.; Xu, L.; Xu, C.; Kotov, N. A. Single- and Multi-Component Chiral Supraparticles as Modular Enantioselective Catalysts. *Nat. Commun.* **2019**, *10*, 4826.

(17) Zhang, H.; Li, S.; Qu, A.; Hao, C.; Sun, M.; Xu, L.; Xu, C.; Kuang, H. Engineering of Chiral Nanomaterials for Biomimetic Catalysis. *Chem. Sci.* **2020**, *11*, 12937–12954.

(18) Wu, F.; Tian, Y.; Luan, X.; Lv, X.; Li, F.; Xu, G.; Niu, W. Synthesis of Chiral Au Nanocrystals with Precise Homochiral Facets for Enantioselective Surface Chemistry. *Nano Lett.* **2022**, *22*, 2915–2922.

(19) Liu, T.; Jin, R.; Yuan, P.; Bai, Y.; Cai, B.; Chen, X. Intracellular Enzyme-Triggered Assembly of Amino Acid-Modified Gold Nanoparticles for Accurate Cancer Therapy with Multimode. *ACS Appl. Mater. Interfaces* **2019**, *11*, 28621–28630.

(20) Zhang, M.; Zhang, H.; Feng, J.; Zhou, Y.; Wang, B. Synergistic Chemotherapy, Physiotherapy and Photothermal Therapy against Bacterial and Biofilms Infections through Construction of Chiral Glutamic Acid Functionalized Gold Nanobipyramids. *Chem. Eng. J.* **2020**, *393*, 124778.

(21) Li, Y.; Miao, Z.; Shang, Z.; Cai, Y.; Cheng, J.; Xu, X. A Visible- and NIR-Light Responsive Photothermal Therapy Agent by Chirality-Dependent MoO_{3-x} Nanoparticles. *Adv. Funct. Mater.* **2020**, *30*, 1906311.

(22) Ayuso, D.; Neufeld, O.; Ordonez, A. F.; Decleva, P.; Lerner, G.; Cohen, O.; Ivanov, M.; Smirnova, O. Synthetic Chiral Light for Efficient Control of Chiral Light–Matter Interaction. *Nat. Photonics* **2019**, *13*, 866–871.

(23) Yan, J.; Feng, W.; Kim, J.-Y.; Lu, J.; Kumar, P.; Mu, Z.; Wu, X.; Mao, X.; Kotov, N. A. Self-Assembly of Chiral Nanoparticles into Semiconductor Helices with Tunable near-Infrared Optical Activity. *Chem. Mater.* **2020**, *32*, 476–488.

(24) Spreyer, F.; Mun, J.; Kim, H.; Kim, R. M.; Nam, K. T.; Rho, J.; Zentgraf, T. Second Harmonic Optical Circular Dichroism of Plasmonic Chiral Helicoid-III Nanoparticles. *ACS Photonics* **2022**, *9*, 784–792.

(25) Lee, H.-E.; Kim, R. M.; Ahn, H.-Y.; Lee, Y. Y.; Byun, G. H.; Im, S. W.; Mun, J.; Rho, J.; Nam, K. T. Cysteine-Encoded Chirality Evolution in Plasmonic Rhombic Dodecahedral Gold Nanoparticles. *Nat. Commun.* **2020**, *11*, 263.

(26) Zhuo, X.; Mychinko, M.; Heyvaert, W.; Larios, D.; Obelleiro-Liz, M.; Taboada, J. M.; Bals, S.; Liz-Marzán, L. M. Morphological and Optical Transitions during Micelle-Seeded Chiral Growth on Gold Nanorods. *ACS Nano* **2022**, *16*, 19281–19292.

(27) Zheng, G.; He, J.; Kumar, V.; Wang, S.; Pastoriza-Santos, I.; Pérez-Juste, J.; Liz-Marzán, L. M.; Wong, K.-Y. Discrete Metal Nanoparticles with Plasmonic Chirality. *Chem. Soc. Rev.* **2021**, *50*, 3738–3754.

(28) Cho, N. H.; Kim, Y. B.; Lee, Y. Y.; Im, S. W.; Kim, R. M.; Kim, J. W.; Namgung, S. D.; Lee, H.-E.; Kim, H.; Han, J. H.; Chung, H. W.; Lee, Y. H.; Han, J. W.; Nam, K. T. Adenine Oligomer Directed Synthesis of Chiral Gold Nanoparticles. *Nat. Commun.* **2022**, *13*, 3831.

(29) Weyland, M.; Midgley, P. A. Electron Tomography. In *Nanocharacterisation*; Kirkland, A. I., Haigh, S. J., Eds.; The Royal Society of Chemistry, 2015; pp 211–299.

(30) Heyvaert, W.; Pedrazo-Tardajos, A.; Kadu, A.; Claes, N.; González-Rubio, G.; Liz-Marzán, L. M.; Albrecht, W.; Bals, S. Quantification of the Helical Morphology of Chiral Gold Nanorods. *ACS Mater. Lett.* **2022**, *4*, 642–649.

(31) Sa, J.; Hu, N.; Heyvaert, W.; Van Gordon, K.; Li, H.; Wang, L.; Bals, S.; Liz-Marzán, L. M.; Ni, W. Spontaneous Chirality Evolved at the Au–Ag Interface in Plasmonic Nanorods. *Chem. Mater.* **2023**, *35*, 6782–6789.

(32) Albrecht, W.; Bals, S. Fast Electron Tomography for Nanomaterials. *J. Phys. Chem. C* **2020**, *124*, 27276–27286.

(33) Vanrompay, H.; Skorikov, A.; Bladt, E.; Béché, A.; Freitag, B.; Verbeeck, J.; Bals, S. Fast versus Conventional HAADF-STEM Tomography of Nanoparticles: Advantages and Challenges. *Ultramicroscopy* **2021**, *221*, 113191.

(34) Hubbard, W. A.; Mecklenburg, M.; Chan, H. L.; Regan, B. C. STEM Imaging with Beam-Induced Hole and Secondary Electron Currents. *Phys. Rev. Appl.* **2018**, *10*, 044066.

(35) Vlasov, E.; Skorikov, A.; Sánchez-Iglesias, A.; Liz-Marzán, L. M.; Verbeeck, J.; Bals, S. Secondary Electron Induced Current in Scanning Transmission Electron Microscopy: An Alternative Way to Visualize the Morphology of Nanoparticles. *ACS Materials Lett.* **2023**, *5*, 1916–1921.

(36) Everhart, T. E.; Wells, O. C.; Matta, R. K. A Novel Method of Semiconductor Device Measurements. *Proc. IEEE* **1964**, *52*, 1642–1647.

(37) Leamy, H. J. Charge Collection Scanning Electron Microscopy. *J. Appl. Phys.* **1982**, *53*, R51–R80.

(38) Duchamp, M.; Hu, H.; Lam, Y. M.; Dunin-Borkowski, R. E.; Boothroyd, C. B. STEM Electron Beam-Induced Current Measurements of Organic-Inorganic Perovskite Solar Cells. *Ultramicroscopy* **2020**, *217*, 113047.

(39) Lin, Y.; Joy, D. C. A New Examination of Secondary Electron Yield Data. *Surf. Interface Anal.* **2005**, *37*, 895–900.

(40) Midgley, P. A.; Weyland, M. 3D Electron Microscopy in the Physical Sciences: The Development of Z-Contrast and EFTEM Tomography. *Ultramicroscopy* **2003**, *96*, 413–431.

(41) Otsu, N. A Threshold Selection Method from Gray-Level Histograms. *IEEE Trans. Syst. Man. Cybern.* **1979**, *9*, 62–66.

(42) Samet, H.; Tamminen, M. Efficient Component Labeling of Images of Arbitrary Dimension Represented by Linear Bintrees. *IEEE Trans. Pattern Anal. Mach. Intell.* **1988**, *10*, 579–586.

(43) van Aarle, W.; Palenstijn, W. J.; De Beenhouwer, J.; Altantzis, T.; Bals, S.; Batenburg, K. J.; Sijbers, J. The ASTRA Toolbox: A Platform for Advanced Algorithm Development in Electron Tomography. *Ultramicroscopy* **2015**, *157*, 35–47.

(44) Mecklenburg, M.; Hubbard, W. A.; Lodico, J. J.; Regan, B. C. Electron Beam-Induced Current Imaging with Two-Angstrom Resolution. *Ultramicroscopy* **2019**, *207*, 112852.

(45) Dyck, O.; Swett, J. L.; Evangeli, C.; Lupini, A. R.; Mol, J.; Jesse, S. Contrast Mechanisms in Secondary Electron E-Beam-Induced Current (SEEBIC) Imaging. *Microsc. Microanal.* **2022**, *28*, 1567–1583.